RSC Advances

PAPER

View Article Online
View Journal | View Issue

Cite this: *RSC Adv.*, 2022, **12**, 4475

Increasing the oxygen-containing functional groups of oxidized multi-walled carbon nanotubes to improve high-rate-partial-state-of-charge performance†

Haining Peng,[a] Li Dong,[b] Shiyuan Gao[b] and Zhenwei Wang *[a]

Multi-walled carbon nanotubes (MWCNTs) with different oxygen functional groups were prepared from hot nitric acid reflux treatment. The acid-treated MWCNTs (a-MWCNTs) were introduced to negative active materials (NAMs) of lead-acid batteries (LABs) and the high-rate-partial-state-of-charge (HRPSoC) performance of the LABs was evaluated. A-MWCNTs with high quantities of carboxylic (COO^-) and carbonyl (C=O) functional groups significantly improve the lead sulfate ($PbSO_4$) reduction to lead (Pb) and thereby improve HRPSoC cycle life. The addition of a-MWCNTs to NAMs is helpful for the formation of larger crystals of ternary lead sulfate (3BS). The improved LABs performance is due to the formation of a sponge crisscrossed rod-like structure at the negative plate in the presence of a-MWCNTs. This unique channels structure is conducive to the diffusion of the electrolyte into the negative plate and delays the $PbSO_4$ accumulation during HRPSoC cycles. The HRPSoC cycle life with a-MWCNTs is significantly prolonged up to the longest cycles of 39 580 from 19 712. In conclusion, oxygen-containing groups on the a-MWCNTs showed significant influence on the curing process and forming process and then improved HRPSoC performance.

Received 26th November 2021
Accepted 23rd January 2022

DOI: 10.1039/d1ra08667g

rsc.li/rsc-advances

1. Introduction

Since their invention by Plante in 1859,[1,2] LABs have all along occupied a leading position in secondary batteries due to their low cost, mature fabrication technology, security, reliability,[3] and recyclability.[4] Working under the HRPSoC continuously, LABs will suffer quick battery failures because of the irreversible sulfation of the negative plates.[5–7] $PbSO_4$ comes into being at the negative plate, hinders electrochemical reactions and causes premature battery failure. Therefore, inhibiting the sulfation of the negative plate under HRPSoC conditions can increase the cycle life of LABs. Adding carbon additives to NAMs is a promising way to alleviate negative plate sulfation and improve the HRPSoC cycle life.[8] The main effects of carbon materials in the negative plate can be summarized in four aspects, as below.[9–12]

(1) Providing additional nucleation sites for small $PbSO_4$ crystals to limit particle growth;[13,14] (2) increasing the electrical conductivity and specific surface area of the active lead to accelerate the electrochemical reaction of Pb^{2+} ions;[15,16] (3) increasing the porosity of NAMs, promoting the diffusion of SO_4^{2-} ions and the combination of SO_4^{2-} and H^+ ions;[9,17] (4) as a buffer, reducing the sulfation phenomenon caused by high current acting on the negative plate.[18] The reaction mechanism of MWCNTs is shown in Fig. 1.

Until now, various types of carbon-based materials have been adopted as additives for NAMs, such as carbon black,[19–22] activated carbon,[23–26] graphite[27–30] and various carbon-based nanomaterials.[31,32] Carbon nanotubes are considered to be most promising new carbon materials for improving the cycle life of HRPSoC due to excellent physical and chemical properties such as it's ordered structure, high conductivity, and chemical stability.[33,34] However, the addition of untreated carbon materials can not meet the requirements of HRPSoC cycle life, so that carbon materials were modified with different functional groups.[35] Cai[36] *et al.*, added graphene oxide (GO) with different oxygen-containing groups to the negative plate. The C–O groups on the GO surface promote the hydrogen evolution reaction at the negative plate and the C=O groups prolong the HRPSoC life. Wang[37] *et al.* modified the surface of activated carbon with acidic and basic groups. The acidic functional groups promote hydrogen evolution while the basic groups can inhibit hydrogen evolution. Therefore, carbon materials modified by basic groups are conducive to prolonging the service life.

As previously published by our team,[38] the concentration of oxygen-containing functional groups of MWCNTs increased significantly after reflux in HNO_3(56%) for 1 hour. The oxygen-

[a]*School of Chemical and Environmental Engineering, Shanghai Institute of Technology, Shanghai, 201418, China. E-mail: wangzhenwei@sit.edu.cn*

[b]*Zhaoqing Leoch Battery Technology Co. Ltd., Guangdong Province, 518000, China*

† Electronic supplementary information (ESI) available. See DOI: 10.1039/d1ra08667g

containing functional groups on MWCNTs can increase the content of 3BS during cured of NAMs. After formation, NAMs present a structure of cross quasi-rod-shaped Pb flakes, which facilitated electron transfer and electrolyte diffusion, consequently advancing the conversion between Pb and $PbSO_4$. Therefore, adding a-MWCNTs to the negative plate considerably extend the HRPSoC cycle life. Until now, few studies have focused on the effect of the relative proportions of different oxygen-containing groups on the surface of MWCNTs on the HRPSoC performance of LABs.

In the present work, MWCNTs will be treated with nitric acid for different times to obtain different C═O, O–C═O, and C–O relative contents. The effects of oxygen functional groups with different relative contents on the physical and chemical properties of the negative plate of LABS will be studied in detail.

2. Experimental

2.1 Chemical and reagents

Lead oxide (PbO) powder (oxidation degree = 72%) and vanisperse A were provided by Zhaoqing Leoch Battery Technology Co. Ltd. (Zhaoqing, China). Vulcan carbon XC-72R (VC-72) was purchased from Cabot Co. Ltd. (Shanghai, China). MWCNTs were purchased from Nanjing XFNANO Materials Tech Co. Ltd. (Nanjing, China). Barium sulfate ($BaSO_4$) and sulfuric acid (H_2SO_4, 98%) were procured from Sinopharm Chemical Reagent Co. Ltd. (Shanghai, China). Unless otherwise specified, reagents were used as received without further purification. Ultrapure water is adopted as water source if necessary in all experiments.

2.2 Preparation of acid-treated MWCNTs

A-MWCNTs were prepared by refluxing 1 g of MWCNTs in 250 ml nitric acid (56%) for 2, 6, 12, and 24 h, respectively. Subsequently, MWCNTs were repeatedly washed with ultrapure water and centrifuged until neutral pH. The samples with different reflux times were marked as MWCNTs-blank, MWCNTs-2 h, MWCNTs-6 h, MWCNTs-12 h, and MWCNTs-24 h. The a-MWCNTs were then re-dispersed in water to obtain an aqueous suspension of 9 mg mL^{-1}.

2.3 Preparation of negative plates

PbO powder (oxidation degree = 72%), conductive carbon black (VC-72), vanisperse A, and $BaSO_4$ were dry mixed and stirred evenly at a mass ratio of 100 : 0.2 : 0.2 : 0.8. A specific volume of 9 mg ml^{-1} a-MWCNTs suspension was dispersed in water and then quickly added to the above dry mixture and stirred to obtain uniform slurry. After mixing for a few minutes, H_2SO_4 (1.4 g cm^{-3}) dropwise was added while stirring to obtain the negative plate paste for coating. The negative plates were prepared by manually coating 6.0 g negative paste on a Pb–Sn–Ca grid (45 mm × 26 mm × 1.6 mm), and then subjected to commercial curation and formation processes. The negative plate samples containing a-MWCNTs with different acid-treatment times were marked as plate-blank, plate-2 h, plate-6 h, plate-12 h, plate-24 h.

The 2 V/0.75 Ah simulated cells were assembled with one negative plate and two commercial positive plates, separated by a 1.5 mm absorbent glass mat (AGM) and H_2SO_4 (9 ml, ρ = 1.28 g cm^{-3}) was used as an electrolyte. Simulated batteries assembled with plate-blank (P-blank), plate-2 h (P-2 h), plate-6 h (P-6 h), plate-12 h (P-12 h), and plate-24 h (P-24 h) negative plates were labeled as Cell-blank, Cell-2 h, Cell-6 h, Cell-12 h, and Cell-24 h. Due to the excessive amount of positive active material, the performance of the simulated battery was determined by the negative plate.

2.4 Physical characterization

Scanning electron microscopy (SEM) images were obtained using a field-emission scanning electron microscope (FE-SEM, Hitachi S-4800). Transmission electron microscopy (TEM) images were acquired using a JEM-200CX transmission electron microscope operated at an acceleration voltage of 120 KeV. Fourier transform infrared spectroscopy (FT-IR) measurements were performed on a Nicolet Avatar370 FT-IR instrument (Thermo Nicolet, USA). Powder X-ray diffraction (XRD) measurements were performed on a 3 KW D/MAX2500V+/PC instruments. X-ray photoelectron spectroscopy images were acquired using a VG Multilab 2000 (the binding energies were calibrated relative to the C_{1s} peak from MWCNTs sample at 284.6 eV).

2.5 Electrochemical measurements

Cyclic Voltammetry (CV) was carried out in H_2SO_4 (1.28 g cm^{-3}) using Metrohm Multi Autolab/M204 potentiostat equipped with a booster. The CV was conducted in a three-electrode configuration using a negative plate as a working electrode, commercial positive plate as counter electrode, and a Hg/Hg_2SO_4 electrode as reference electrode. CV measurements were carried out at room temperature in the potential window of 0 to −1.6 at 1 mV s^{-1}. Electrochemical impedance spectroscopy (EIS) was performed at the open circuit potential (OCP) with a frequency ranging from 0.1 Hz to 10 kHz with an amplitude of 5 mV.

2.6 HRPSoC cycle test of the simulated cells

Before the tests, the cells were first activated according to the multi-step charge/discharge protocol provided by the factory. The discharge capacities were obtained at a constant discharge current of 0.05C to a cut-off voltage of 1.75 V.

Peukert plot was obtained by measuring the capacities of the simulated cell at different currents to determine the 1C current for HRPSoC tests. The cells were charged at a constant current of 0.1C up to the voltage of 2.45 V, followed by the floating charge at a constant voltage of 2.45 V for another 18 h. The cell performance was evaluated under the simulated HRPSoC condition, using a simplified imitating micro-hybrid driving mode. After fully charged, the cell was discharged at a current of 1C to 50% state of charge (SoC) and then subjected to cycling according to the following module: charging at 1C rate for 30 s, rest for 10 s, discharging at 1C rate for 30 s, rest for 10 s. The test was stopped when the end-of-discharge voltage ($V_{discharge}$) fell to 1.6 V or when the end-of-charge voltage (V_{charge}) rose to 2.83 V. And the first cycle-set, the simulated batteries were torn down, and the NAMs were collected for characterization.

3. Result and discussion

3.1 Characterisation of acid-treated MWCNTs

The MWCNTs are reflux in nitric acid for several hours to obtain various contents of oxygen-containing groups. In Fig. 1A_I–E_I, the morphology of MWCNTs not change significantly. Even if the acid treatment time is up to 24 hours, it will not lead to the fracture of MWCNTs. This treatment method not only kept the original physical properties of MWCNTs, but also changed their oxidation degree, which is more beneficial to study the effect of oxidation degree on electrochemical performance.

Fig. 2F displays the Raman spectra of pristine and various a-MWCNTs. The relative intensity of the D band to G band (I_D/I_G) reveals the change of the electronic conjugation and represents the disorder of sp^2-hybridized carbon materials. The I_D/I_G value of pristine MWCNTs is 0.72, and it increased to 1.11 (MWCNTs-2 h), 1.68 (MWCNTs-6 h), 1.69 (MWCNTs-12 h), and 1.80 (MWCNTs-24 h), respectively. Therefore, the increase of the I_D/I_G value with the refluxing time can be attributed to the increase in oxygen functionalities on MWCNTs. The intensity of the D′ band is also related to the oxygen functionalities on MWCNTs.[39] The D′ band is similar to the D band, which occurs *via* an intravalley double-resonance process in the presence of defects. And the acid refluxing introduced plenty of oxygen functionalities onto MWCNTs, which created large amounts of defects.[40]

The effects of the a-MWCNTs are also analyzed by FT-IR. In Fig. 2G, the peak at 1725 cm^{-1} is related to the stretching vibration of C=O, the peak at 1623 cm^{-1} and 1563 cm^{-1} are due to the skeleton vibration of carbon rings and C=C stretching mode respectively. The peak at 1382 cm^{-1} is attributed to the O–H stretching vibration of carboxyl groups, and the peak at 1213 cm^{-1} corresponds to the stretching vibration of C–O. And the peaks at 1725, 1382, 1213 cm^{-1} become much more pronounced after the acid refluxing, indicating that large amounts of oxygen-containing functionalities have been incorporated onto a-MWCNTs.

XPS measurements are also performed to analyze the change of chemical composition with refluxing time.[41] In Fig. 2A_{II}, the XPS spectrum contain O (1.4%) and C (98.6%). The concentration of O increases with the increasing refluxing time and reached 10.21% for MWCNT-24. As the acid treatment time continues to increase, the peak intensity of O 1s gradually increases. That is to say, the content of oxygen-containing groups on MWCNTs gradually increases.

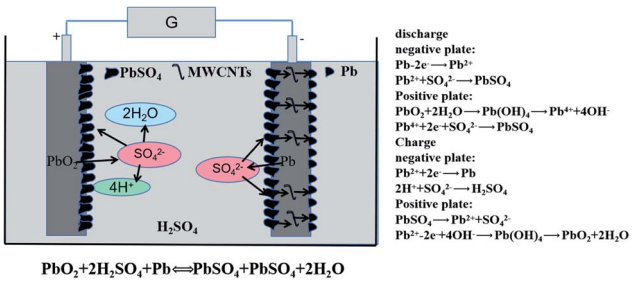

Fig. 1 Schematic diagram of reaction principle of lead-carbon battery.

As shown in the XPS spectrum analysis of C 1s of the MWCNTs sample in Fig. 2, the MWCNTs samples have five types of carbon bonds: C=C (284.6 eV), C–C (285.4 eV ± 0.1 eV), C–O (286.6 ± 0.1 eV), C=O (287.8 eV), and O–C=O (289.0 ± 0.1 eV).[42] The relative content of each oxygen-containing functional group (C–O, C=O, O–C=O) and intact carbon C–C/C=C are used to obtain the relative content of each oxygen-containing functional group (I_{C-O}, $I_{C=O}$, $I_{O-C=O}$). After acid treatment, the relative content of C–O of MWCNTs from 0.62% increased to 4.56%. It shows that the acid treatment can effectively improve the relative content of C–O. The $I_{C=O}$ on MWCNTs-blank is only 0.08%, MWCNTs-2 h is increased to 2.25%, and MWCNTs-6 h is greatly increased to 2.57%, reaching the maximum value. After that, the relative content of the C=O decreases with the acid treatment time.

To study the influence of oxygen-containing functional groups on the electrochemical performance, the relative content and result of $I_{C=O}$, I_{C-O}, $I_{O-C=O}$ are given in Table 1. C=O and O–C=O changed synchronously with the extension of acid treatment time, therefore, these two functional groups have synergistic effects. The $I_{O-C=O} + I_{C=O}$ on MWCNTs-blank is only 0.31%, MWCNTs-2 h is significantly increases to 4.67%, MWCNTs-6 h continue to rise it's peak of 5.24%. With the extension of acid treatment time, the value decreased gradually.

3.2 Effect of MWCNTs on the cured negative active materials (NAMs)

The effect of MWCNTs on the composition and content of each component of the cured NAMs is studied by XRD. Fig. 3A shows that the main components of curing NAMs are as follows: α-PbO, $3PbO \cdot PbSO_4 \cdot H_2O$ (3BS) and $Pb_{10}(CO_3)_6O(OH)_6$ (lead hydrocarbonate, LH).[43,44] By analyzing the intensity of the strongest diffraction peak of each crystal, the relative content of each component can be achieved, as shown in Fig. S2.† The LH percentage in P-blank is 2.73%, the LH is from the reaction between $Pb(OH)_2$ and CO_2 in the air or the oxygen-containing groups on the surface of VC-72. After a-MWCNTs are added to NAMs, the percentage of LH began to decrease, which means that a-MWCNTs can inhibit the reaction of $Pb(OH)_2$ and CO_2 with VC-72. A-MWCNTs have a strong effect on the chemical reactions during the curing process. The proportion of 3BS in plate-blank is only 20.76%, plate-2 h increased to 21.72%, and plate-6 h to 26.02%. However, when MWCNTs-12 h is added to NAMs, the proportion of 3BS began to drop to 22.09%, and plate-24 h further dropped to 21.11%. The $I_{C=O} + I_{O-C=O}$ on MWCNTs promotes the increase of 3BS content during the curing process.[45]

Morphology of the NAMs after curing is analyzed by SEM, as shown in Fig. 3B_I–F_I. The NAMs in the plate-blank are composed of 3BS rods and PbO particles, the PbO particles are scattered irregularly in the 3BS rods. However, adding a-MWCNTs to the negative plate, the size and content of 3BS increases significantly with the relative content of C=O and O–C=O increased. From Fig. 3C_I, the size of 3BS crystals are larger and uniform than plate-blank. The size of the 3BS rod of

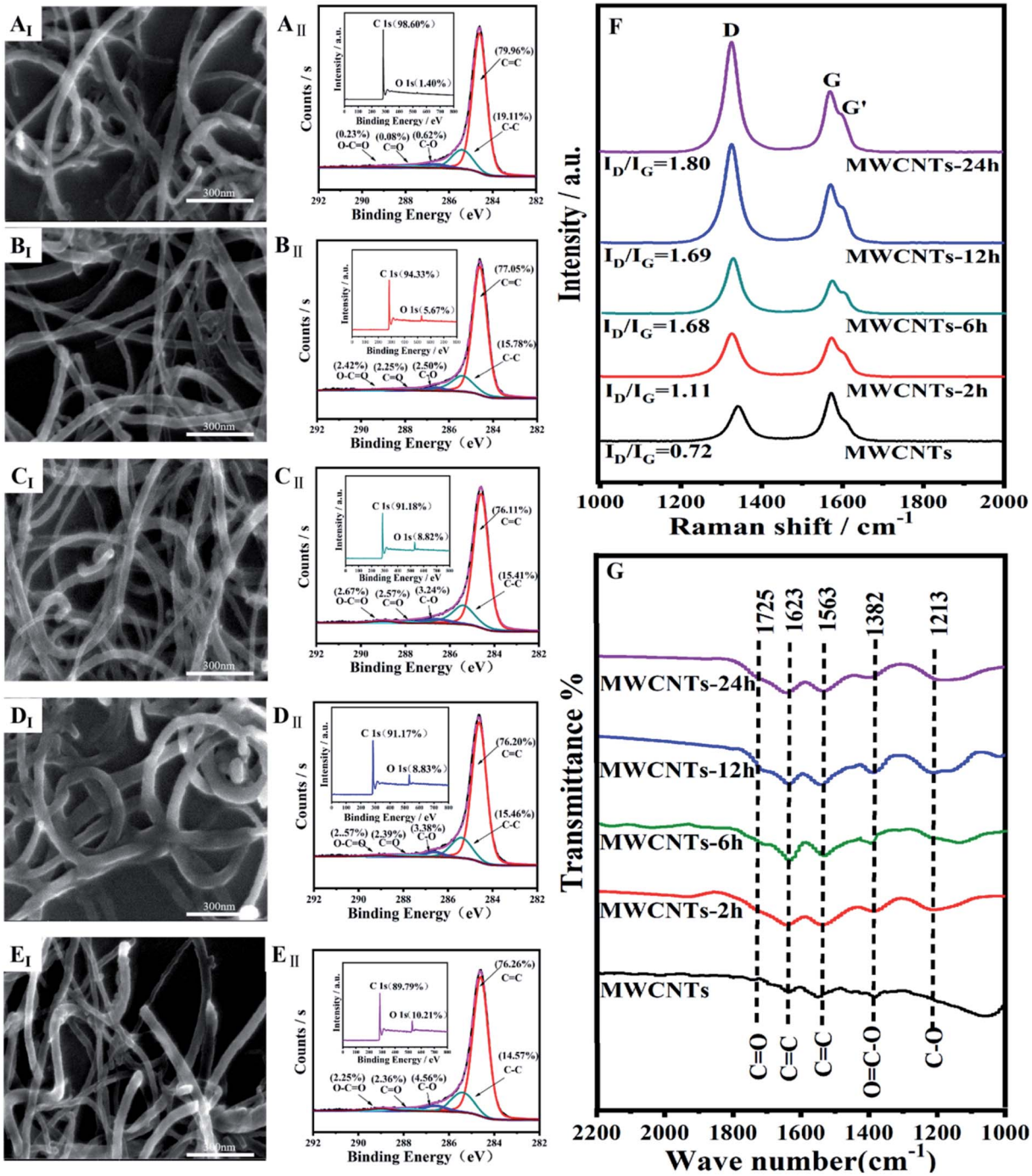

Fig. 2 SEM images (I) and XPS spectra (II) of different carbon samples: MWCNTs (A), MWCNTs-2 h (B), MWCNTs-6 h (C), MWCNTs-12 h (D) and MWCNTs-24 h (E). Raman spectra (F) and FTIR spectra (G) of different MWCNTs.

plate-6 h is obviously increases, in Fig. $3D_I$, and only a very small amount of fine PbO particles can be observed in the middle of the 3BS lead rod. The length of the 3BS rod of plate-12 h has become shorter in Fig. $3E_I$. The content of PbO particles has increases from 71.45% to 76.61%, and the disordered accumulation blocks the pores of NAMs. However, when MWCNTs-24 h is introduced to NAMs, the length of the 3BS rod is further shortened and more PbO particles are observed in Fig. $3F_I$.

3.3 Effect of MWCNTs on the formation NAMs

The formation process is a key process in the forming of negative plate. This process can convert all lead substances into electroactive lead, the porous rod structure is more conducive to the subsequent electrochemical reaction. The effect of a-MWCNTs on the formation stage of the negative plate is studies by XRD, as shown in Fig. 3G. The XRD pattern shows

Table 1 Relative proportion of oxygen-containing groups on the surface of different MWCNTs samples ($I_{C=O}/I_{C-O}$)

Functional group	Blank	2 h	6 h	12 h	24 h
$I_{C=C}$	79.96%	77.05%	76.11%	76.20%	76.26%
I_{C-C}	19.11%	15.78%	15.41%	15.46%	14.57%
I_{C-O}	0.62%	2.50%	3.24%	3.38%	4.56%
$I_{C=O}$	0.08%	2.25%	2.57%	2.39%	2.36%
$I_{O-C=O}$	0.23%	2.42%	2.67%	2.57%	2.25%
$I_{O-C=O} + I_{C=O}$	0.31%	4.67%	5.24%	4.96%	4.61%
I_{C-O}/I_{CC}	0.62%	2.69%	3.54%	3.68%	5.02%
$I_{C=O}/I_{CC}$	0.08%	2.42%	2.80%	2.60%	2.59%
$I_{O-C=O}/I_{CC}$	0.23%	2.60%	2.92%	2.80%	2.48%

that after formation, the PbO, 3BS, and LH crystals in the NAMs are all convertes to sponge lead.

Fig. $3B_{II}$–F_{II} is SEM image of NAMs after formation. Fig. $3D_{II}$ shows that the NAMs present a sponge-like structure, the one-dimensional (1D) structure of Pb rods provides the channel for electron transfer and contributes to the rapid entry of electrolyte inside the negative plate.[38] These will be more conducive to the mutual transformation between Pb and $PbSO_4$, thus delaying the sulfation of the negative plate. From Fig. $3B_{II}$, the structure of the sponge lead of the plate-blank is similar to the precursor of the lead rod and no obvious rod structure is formed. From Fig. $3C_{II}$–F_{II}, a-MWCNTs are introduced to the negative plate, the NAMs is composed of rod-shaped Pb interconnected, and the content and size of rod-shaped Pb increase with the increase of acid treatment time. In Fig. $3C_{II}$, The morphology of sponge lead did not change greatly, but the size of lead rod increased slightly. MWCNTs-6 h is added to the negative plate, the structure of NAMs is loose and showed a trend of elongation, and the rod-like structure of the plate is more obvious. The vertically upward lead rods not only have more pores but also crisscross between the lead rods to form a relatively stable spatial structure, as shown in Fig. $3D_{II}$. From Fig. $3E_{II}$, the size of NAMs increases and the porosity decreases obviously, which hinders the diffusion of electrolyte in the negative plate. For plate-24 h, the size of the lead rod further increased, the boundaries between the lead rods become blurred, and lead rods fuse with each other. This lead rod structure is hindered to the rapid transfer of electrons, and the pores between the lead rods are almost covered. The porosity of NAMs decreases further, electrolyte diffusion becomes more difficult, as shown in Fig. $3F_{II}$.

3.4 Electrochemical properties of the negative plate

Fig. 4A shows the EIS of different negative plate samples, to study the charge transfer resistance (R_{ct}) of the negative plate. The high frequency region and middle frequency region of the curve correspond to the interface impedance and reaction impedance respectively, and the diameter of the semicircle reflects the charge transfer resistance.[46] The semicircle diameter of plate-6 h is the smallest, which indicates that the R_{ct} of the plate-6 h is the smallest. This can be attributed to the intercrossed quasi-rod structure of the NAMs and this structure can accelerate the electrochemical redox reaction between $PbSO_4$ and Pb. For plate-12 h, the electrochemical reaction impedance increased further, due to the further increase of the lead rod size. The pore structure is reduced and the electrolyte is limited to enter the negative plate to participate in the

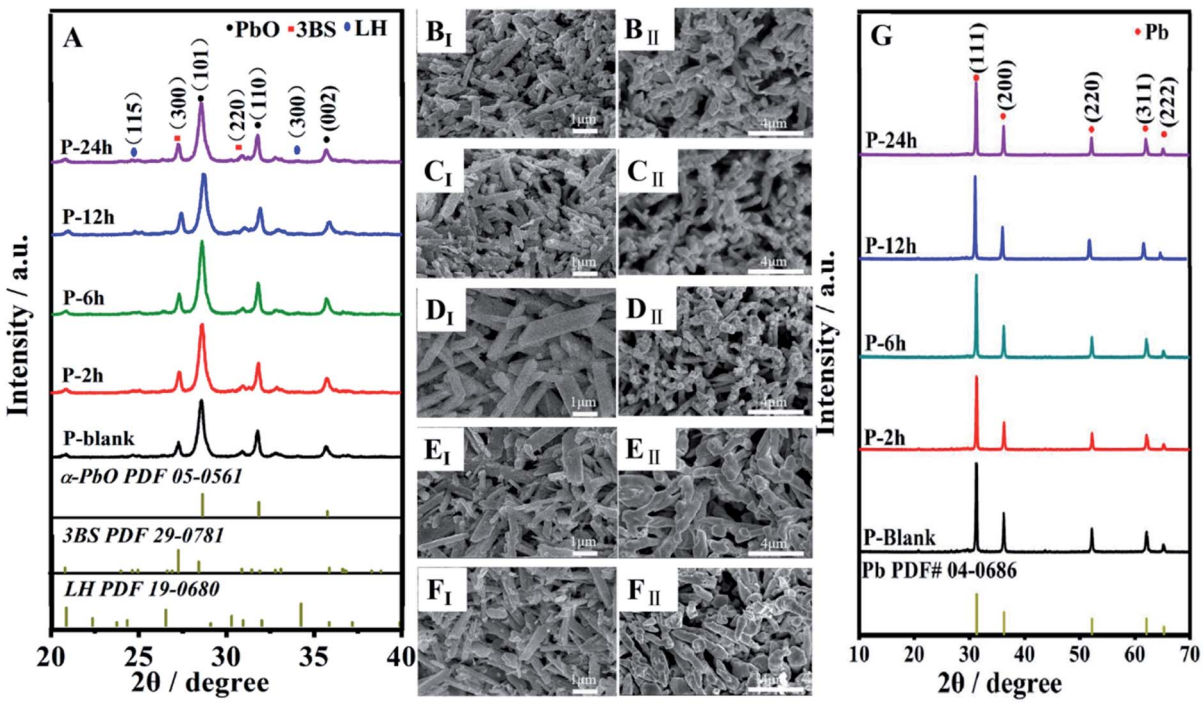

Fig. 3 XRD patterns of the NAM in curing (A) and in formed (G) negative plate. SEM images of the NAM in curing (I) and in formed (II) negative plate added with different carbon material: plate-blank (B), plate-2 h (C), plate-6 h (D), plate-12 h (E), plate-24 h (F).

electrochemical redox reaction. And for plate-24 h, The rods grow in size and fuse with each other, clogging the pores of the NAMs. Such incomplete lead rod structure hinders the rapid transfer of electrons, so the R_{ct} is also greater.

Fig. 4B presents the cyclic voltammograms (CVs) of the negative plates are recorded in a three-electrode system. From Fig. 4, there is a pair of redox peaks on the CV curve, the oxidation peak represents Pb $\rightarrow$ $PbSO_4$, and the reduction peak is the represents $PbSO_4$ $\rightarrow$ Pb.[47,48] When a-MWCNTs are introduce to the negative plate, the peak potential in CV curve has obvious displacement, and the peak value of current increases. Indicate that the addition of a-MWCNTs can promote the $PbSO_4$ $\rightarrow$ Pb oxidation reaction. The NAMs structure of plate-6H is composes of interconnected rod-like Pb, which provides a channel for rapid electron transfer, thus promoting the redox reaction between $PbSO_4$ and Pb. For plate-12 h, due to the increase in the size of the lead rod, the pores of the NAMs are reduces and the transfer between charges becomes difficult, resulting in the reduction of the redox reaction rate. Because the boundaries of the lead rods of plate-24 h are fuses with each other, and the pores of the NAMs are covered, this structure impedes the rapid transfer of electrons between the NAMs.

The simulated battery is assembled by one negative plate and two commercial positive plates to ensure that the performance of the simulated battery is only determined by the negative plate. The initial capacity is evaluated by charging and discharging for 3 cycles at a constant current of 0.05C in the voltage range of 2.4–1.75 V. Fig. 4C records the charging and discharging curve of the simulated battery in the third cycle. The capacity of the plate-blank is only 0.6257 mA h, after adding a-MWCNTs, the capacity of the negative plate increases. The capacitance of plate-6 h is the largest, due to the crisscross lead rod structure is more conducive to the electrolyte entering the interior of the negative plate. The resistance to charge transfer is reduced, so the capacitance of the plate-6 h is higher than other negative plates. On the hand, the size of the lead rod of plate-12 h grown further, making it difficult for the electrolyte to enter the interior of the electrode plate, which reduce the redox reaction rate between Pb and $PbSO_4$. As a result, lead sulfate cannot be quickly convertes to lead and accumulates on the surface and inside the negative plate, resulting in a greatly reduces capacity of the negative plate.[49,50]

3.5 Tests of the simulated cells

Fig. 4D shows $V_{discharge}$ as a function of cycle number of each cell. The HRPSoC cycle life of the simulated battery increased with the increase of the $I_{C=O}$ + $I_{O-C=O}$ value on MWCNTs. A-

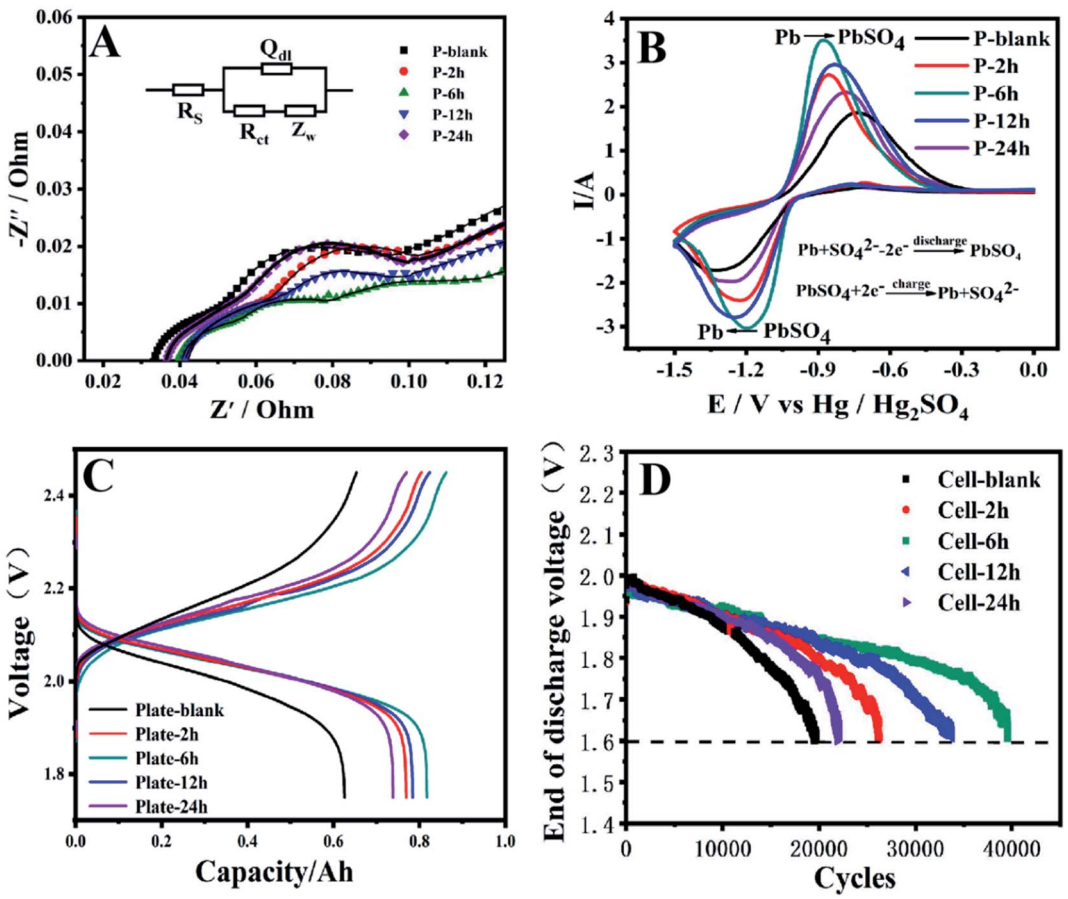

Fig. 4 (A) Nyquist plots of the negative plates in H_2SO_4 (1.28 g cm^{-3}). (B) CV curves of the negative plates in H_2SO_4 (1.28 g cm^{-3}); (C) capacity curves of the negative plates in H_2SO_4 (1.28 g cm^{-3}); (D) the change of the $V_{discharge}$ as a function of cycle number under HRPSoC condition for the simulated cells within the first HRPSoC cycle-set.

MWCNTs are introduce to the negative plate, the HRPSoC cycle life is improved that indicates that oxygen-containing groups on a-MWCNTs has a positive effect on the HRPSoC cycle performance of the battery. The morphology of NAMs can be influenced by the oxygen-containing groups on the surface of MWNTs, which results in the formation of pores, conducive to charge transfer and the transformation of Pb and $PbSO_4$. The acid treatment time reaches 2 hours, $I_{C=O} + I_{O-C=O}$ is rapidly increases from 0.31% to 4.67%. The HRPSoC cycle life of Cell-2h is 26 226, a 130% improvement, indicating that short acid-treatment can effectively improve the cycle life of the battery. The HRPSoC cycle life of Cell-6 h with the highest $I_{C=O} + I_{O-C=O}$ is 39 580, which is 2.01 times that of Cell-blank. The excellent HRPSoC cycle performance is attributed to its unique cross-lead rod structure, which provides more channels for charge transfer, promoting the redox reaction between Pb and $PbSO_4$. The $I_{C=O} + I_{O-C=O}$ on MWCNTs-12 h is lower than that of MWCNTs-6 h, and the HRPSoC cycle life of Cell-12 h is reduced to 33 764 cycles. The increase in the size of the lead rod of Plant-12 h leads to a decrease in the pores of the NAMs, it will prevent the electrolyte from entering the negative plate, thus reducing the cycle life of HRPSoC. The $I_{C=O} + I_{O-C=O}$ on MWCNTs-24 h is further decreased, the HRPSoC cycle life is reduced to only 21 915 cycles. The lead rods are fused to cover the pores of the NAMs, inhibiting the rapid transfer of electrons and the redox reaction between Pb and $PbSO_4$. Therefore, the $I_{C=O} + I_{O-C=O}$ on MWCNTs is relatively high, which is beneficial to improve the HRPSoC cycle life of the battery.

After the HRPSoC cycle test, the simulated battery is dissected and the negative plate is taken out. NAMs are collected for XRD and SEM tests to analyze the composition and morphology. Fig. 5G shows the XRD pattern of NAMs collected inside the negative plate after the HRPSoC cycle test. NAMs are composes of Pb and $PbSO_4$ crystals, from Fig. 5F, the percentage of $PbSO_4$ in the plate-blank is 62.37%. The addition of a-MWCNTs can effectively reduce the proportion of $PbSO_4$, indicating that the oxygen-containing functional groups on MWCNTs alleviate the accumulation of $PbSO_4$. The percentage of $PbSO_4$ in NAMs decreases with the increase of $I_{C=O} + I_{O-C=O}$ on MWCTNs, the proportion of $PbSO_4$ in plate-2 h dropped to 56.63%, which is 5.74% lower than that of plate-blank. The percentage of $PbSO_4$ in plate-6 h dropped to only 28.58%, which can be attributed to the staggered lead rod structure of NAMs. This structure is beneficial to promote the electrochemical reaction kinetics, thereby delaying the $PbSO_4$ accumulation. The $I_{C=O} + I_{O-C=O}$ on MWCNTs-12 h began to decrease, and the content of $PbSO_4$ in the negative plate began to increase. The $PbSO_4$ content of plate-24 h is as high as 60.37%, the lead rods are fused to cover the pores of the NAMs, this structure hinders electron transfer and electrolyte diffusion, which is not conducive to the reduction of $PbSO_4$ to Pb.

Fig. 5A–E is an SEM image of the NAMs after the HRPSoC cycle test. From Fig. 5A that the NAMs of plate-blank exist large-sized $PbSO_4$ particles. In contrast, adding a-MWCNTs to the negative plate can inhibit the growth of $PbSO_4$ particle size to varying degrees, as shown in Fig. 5B–E. The NAMs morphology inside plate-2 h shown in Fig. 5B, the size of the $PbSO_4$ particles is significantly reduced, and some small Pb particles begin to appear around the $PbSO_4$ particles, which indicates that the sulfation of the negative plate has been alleviated. The size of

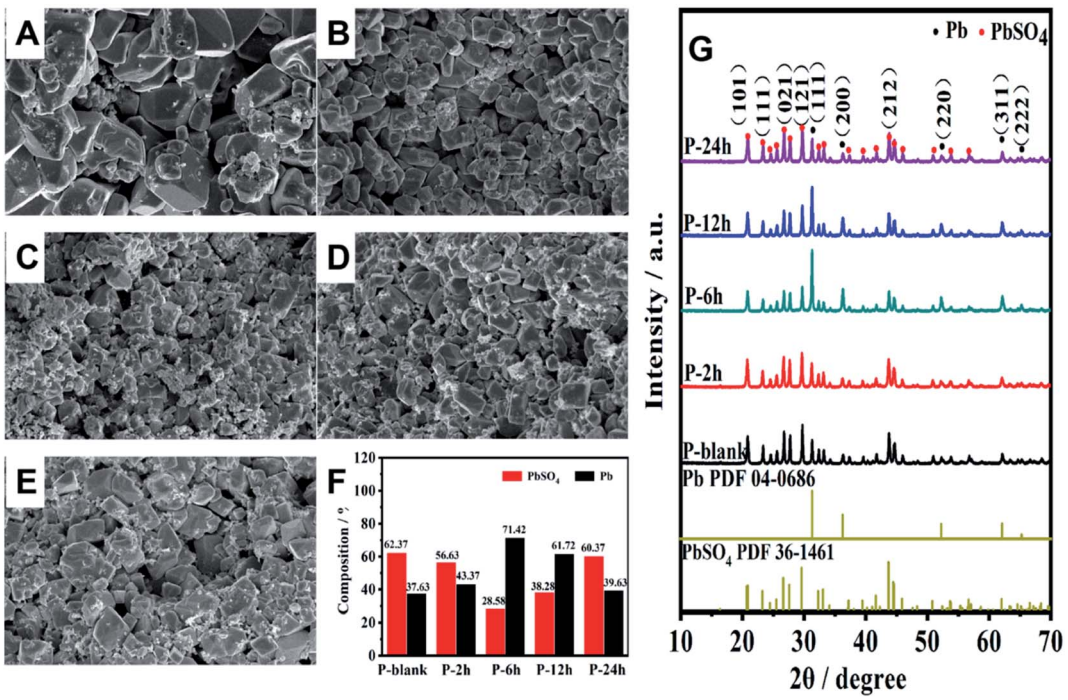

Fig. 5 SEM images of the NAMs in the interior of the negative plates after the first HRPSoC cycle-set: plate-blank (A), plate-2 h (B), plate-6 h (C), plate-12 h (D), and plate-24 h (E). XRD patterns (G) and compositions (F) of the NAMs collected from the interior of negative plates after the HRPSoC cycle-set.

$PbSO_4$ continues to decrease in the SEM image of plate-6 h, a large number of small Pb particles are surrounded by $PbSO_4$ particles, and the size of $PbSO_4$ is further reduced, as shown in Fig. 4C. In Fig. 4D, the size of $PbSO_4$ began to increase again, and the content of small Pb particles decreased. When MWCNTs-24 h is added to the negative plate, large-size PbSO4 crystals can be seen in the SEM image, as shown in Fig. 4E.

4. Conclusion

In this study, MWCNTs with different relative contents of oxygen-containing groups are used as additives to study the effect on the cyclic performance of negative plate. The content of $I_{C=O} + I_{O-C=O}$ on the MWCNTs-6 h relates to the cycle performance and reached the highest point of 5.24%. In this condition, the staggered Pb rod morphology in the formed NAMs is beneficial to provide channels for rapid electron transfer and electrolyte diffusion, accelerate the conversion between Pb and $PbSO_4$, and effectively delay the accumulation of $PbSO_4$. The cycle life of the simulated battery under HRPSoC reached 39 580 cycles, twice of 19 712 cycles for the battery containing untreated MWCNTs. Therefore, a-MWCNTs with high $I_{C=O} + I_{O-C=O}$ as carbon additives in the negative plate can increase the cycle life of LAB under HRPSoC.

Conflicts of interest

There are no conflicts to declare.

References

1 S.-W. Jeong and B.-K. Ku, *Journal of Oil & Applied Science*, 2014, **31**, 197–202.
2 Z. Li, Z. Wang and L. Wang, *E3S Web Conf.*, 2020, **185**, 01058.
3 S. Sahoo, P. Walke, S. K. Nayak, C. S. Rout and D. J. Late, *Nano Res.*, 2021, **14**, 3669–3689.
4 P. W. Appel and D. B. Edwards, *Adv. Perform. Mater.*, 1996, **3**, 43–55.
5 O. J. Dada, *J. Energy Storage*, 2019, **23**, 579–589.
6 L. Lam, N. Haigh, C. Phyland and A. Urban, *J. Power Sources*, 2004, **133**, 126–134.
7 L. Lam, R. Louey, N. Haigh, O. Lim, D. Vella, C. Phyland, L. Vu, J. Furukawa, T. Takada and D. Monma, *J. Power Sources*, 2007, **174**, 16–29.
8 P. Moseley, *J. Power Sources*, 2009, **191**, 134–138.
9 P. Moseley, R. Nelson and A. Hollenkamp, *J. Power Sources*, 2006, **157**, 3–10.
10 P. T. Moseley, D. A. Rand, A. Davidson and B. Monahov, *J. Energy Storage*, 2018, **19**, 272–290.
11 A. G. Pandolfo and A. F. Hollenkamp, *J. Power Sources*, 2006, **157**, 11–27.
12 D. Pavlov, P. Nikolov and T. Rogachev, *J. Power Sources*, 2010, **195**, 4444–4457.
13 J. Xiang, P. Ding, H. Zhang, X. Wu, J. Chen and Y. Yang, *J. Power Sources*, 2013, **241**, 150–158.
14 R. Shapira, G. D. Nessim, T. Zimrin and D. Aurbach, *Energy Environ. Sci.*, 2013, **6**, 587–594.
15 D. Pavlov, T. Rogachev, P. Nikolov and G. Petkova, *J. Power Sources*, 2009, **191**, 58–75.
16 M. Rahmanifar, *Electrochim. Acta*, 2017, **235**, 10–18.
17 D. Pavlov, P. Nikolov and T. Rogachev, *J. Power Sources*, 2011, **196**, 5155–5167.
18 A. S, M. K. S, K. U. V. Kiran and S. Mayavan, *J. Energy Storage*, 2020, **32**, 101763.
19 H. Dietz, J. Garche and K. Wiesener, *J. Appl. Electrochem.*, 1987, **17**, 473–479.
20 K. Ding, X. Gao, J. Han, C. Li, X. Shi, H. Wang, H. Dou, Z. Guo, Y. Liu and J. Pan, *Int. J. Electrochem. Sci.*, 2019, **14**, 516–530.
21 H.-Y. Hu, N. Xie, C. Wang, F. Wu, M. Pan, H.-F. Li, P. Wu, X.-D. Wang, Z. Zeng and S. Deng, *Appl. Sci.*, 2019, **9**, 186.
22 H. Yang, Y. Qiu and X. Guo, *Electrochim. Acta*, 2017, **235**, 409–421.
23 S. Arun, K. U. V. Kiran, S. M. Kumar, M. Karnan, M. Sathish and S. Mayavan, *J. Energy Storage*, 2021, **34**, 102225.
24 B. Hong, X. Yu, L. Jiang, H. Xue, F. Liu, J. Li and Y. Liu, *RSC Adv.*, 2014, **4**, 33574–33577.
25 Z. Lin, W. Zhang, N. Lin, H. Lin and J. Shi, *ChemistrySelect*, 2020, **5**, 2551–2558.
26 P. Tong, R. Zhao, R. Zhang, F. Yi, G. Shi, A. Li and H. Chen, *J. Power Sources*, 2015, **286**, 91–102.
27 M. Fernández, J. Valenciano, F. Trinidad and N. Muñoz, *J. Power Sources*, 2010, **195**, 4458–4469.
28 Y.-I. Jang, N. J. Dudney, T. N. Tiegs and J. W. Klett, *J. Power Sources*, 2006, **161**, 1392–1399.
29 J. Kosacki and F. Dogan, *J. Electrochem. Soc.*, 2021, **168**, 030513.
30 L. Wang, H. Zhang, W. Zhang, G. Cao, H. Zhao and Y. Yang, *Mater. Lett.*, 2017, **206**, 113–116.
31 J. Yin, Z. Lin, D. Liu, C. Wang, H. Lin and W. Zhang, *J. Electroanal. Chem.*, 2019, **832**, 152–157.
32 X. Zou, Z. Kang, D. Shu, Y. Liao, Y. Gong, C. He, J. Hao and Y. Zhong, *Electrochim. Acta*, 2015, **151**, 89–98.
33 A. Banerjee, B. Ziv, Y. Shilina, E. Levi, S. Luski and D. Aurbach, *ACS Appl. Mater. Interfaces*, 2017, **9**, 3634–3643.
34 M. Blecua, E. Fatas, P. Ocon, B. Gonzalo, C. Merino, F. de la Fuente, J. Valenciano and F. Trinidad, *Electrochim. Acta*, 2017, **257**, 109–117.
35 M. Kandasamy, S. Sahoo, S. K. Nayak, B. Chakraborty and C. S. Rout, *J. Mater. Chem. A*, 2021, **9**, 17643–17700.
36 W. Cai, K. Qi, Z. Chen, X. Guo and Y. Qiu, *J. Energy Storage*, 2018, **18**, 414–420.
37 J. J. Wang, L. Dong, M. M. Liu, J. Y. Wang, Q. S. Shao, A. J. Li, W. Yan, J. C. Y. Jung and J. J. Zhang, *J. Energy Storage*, 2020, **29**, 101325.
38 L. Dong, C.-H. Chen, J.-Y. Wang, H.-W. Li, H. Zheng, W. Yan, J. C.-Y. Jung and J. J. Zhang, *RSC Adv.*, 2021, **11**, 15273–15283.
39 J. F. Cardenas, *Carbon*, 2008, **46**, 1327–1330.
40 Y. Hu, J. Yang, J. Hu, J. Wang, S. Liang, H. Hou, X. Wu, B. Liu, W. Yu and X. He, *Adv. Funct. Mater.*, 2018, **28**, 1870056.
41 H. Yang, K. Qi, L. Gong, W. Liu, S. Zaman, X. Guo, Y. Qiu and B. Y. Xia, *ACS Sustainable Chem. Eng.*, 2018, **6**, 11408–11413.

42 A. Mansuroglu, M. B. Arvas, C. Kiraz, B. Sayhan, A. Akgumus, M. Gencten, M. Sahin and Y. Sahin, *J. Electrochem. Soc.*, 2021, **168**, 060512.
43 N. Sugumaran, P. Everill, S. W. Swogger and D. Dubey, *J. Power Sources*, 2015, **279**, 281–293.
44 M. Venkateswarlu, *J. Energy Power Eng.*, 2015, **9**, 190882.
45 G. Petkova, P. Nikolov and D. Pavlov, *J. Power Sources*, 2006, **158**, 841–845.
46 Y. Jiang, H. Zhu, C. Yu, X. Cao, L. Cheng, R. Li, S. Yang and C. Dai, *Int. J. Electrochem. Sci.*, 2017, **12**, 10882–10893.
47 J. Lach, K. Wróbel, J. Wróbel, P. Podsadni and A. Czerwiński, *J. Solid State Electrochem.*, 2019, **23**, 693–705.
48 J. Lian, W. Li, F. Wang, J. Yan, K. Wang, S. Cheng and K. Jiang, *J. Electrochem. Soc.*, 2017, **164**, A1726.
49 D. Pavlov, *J. Power Sources*, 1993, **42**, 345–363.
50 M. Vyas, M. Jain, K. Pareek and A. Garg, *Measurement*, 2019, **148**, 106904.